# Supporting information

# Edge-Site Nanoengineering of $WS_2$ by Low-Temperature Plasma- Enhanced Atomic Layer Deposition for Electrocatalytic Hydrogen Evolution

Shashank Balasubramanyam,[†] Mahdi Shirazi,[†] Matthew A. Bloodgood,[†] Longfei Wu,[‡] Marcel A. Verheijen,[†,§] Vincent Vandalon,[†] Wilhelmus M. M. (Erwin) Kessels,[†] Jan P. Hofmann,[‡] and Ageeth A. Bol[*,†]

[†]*Department of Applied Physics and* [‡]*Laboratory for Inorganic Materials and Catalysis, Department of Chemical Engineering and Chemistry, Eindhoven University of Technology, 5600 MB Eindhoven, The Netherlands*

[§]*Eurofins Materials Science Netherlands B.V., High Tech Campus 11, 5656 AE Eindhoven, The Netherlands*

[*]*a.a.bol@tue.nl*

## Contents

Impact of plasma gas mixture on film properties ........ 2
$WS_2$ PEALD saturation curves ........ 4
XPS analysis ........ 5
Optical emission spectroscopy of the $H_2S$ based plasmas ........ 6
Computational Section ........ 7
(a) Computational details ........ 7
(b) Adsorption of W precursor on the basal plane – {001} facet ........ 8
(c) Complementary Calculations: Proton transfer and reduction of $WS_2$ edge structure .. 9
TEM images of $WS_2$ ($t_{App}$~64 nm) synthesised using $H_2$+$H_2S$ process ........ 11
Film properties of $WS_2$ ($t_{App}$~64 nm) synthesised using $H_2$+$H_2S$ process ........ 12
Copper UPD – evaluation of the number of active sites ........ 12
Surface morphology of $WS_2$ on different substrates ........ 13
Blocking of layers in $WS_2$ film ........ 14
Electrochemical impedance spectroscopy data ........ 14

## Impact of plasma gas mixture on film properties

The flow rate of the gases ($H_2S$ and $H_2$) into the plasma source during the plasma co-reactant step of the PEALD cycle was varied and its impact on the $WS_2$ film properties (morphology and crystallinity) was investigated. As a starting point, $WS_2$ was deposited with an optimized $H_2S$ gas flow of 10 sccm and, subsequently, the $H_2S$ gas was diluted with $H_2$ gas. Figure S1 shows the SEM images of $WS_2$ (after 200 ALD cycles) deposited with (a) $H_2S$ and with (b-e) different flow rates of $H_2$ diluted $H_2S$ plasma gas mixture. $WS_2$ films deposited with $H_2S$ plasma (Figure S1a) appeared to consist of nanoflakes with individual flake sizes in the range of ~10-20 nm. Doubling the $H_2S$ flow rate to 20 sccm had no significant impact on the morphology (data not shown). Dilution of $H_2S$ with $H_2$ gas (30% dilution, $H_2$-$H_2S$: 3-7 sccm, Figure S1b), seemed to cause a slight increase in the nanoflake's size and also cause a reduction in the number of flakes. The $WS_2$ films deposited with both of these plasma gas mixtures exhibited a strong (002) peak in the XRD diffractogram (Fig S1f), suggesting the growth of crystalline $WS_2$ with preferential orientation (with respect to powder diffractogram shown in Figure 4a of the main text).

Increasing the $H_2$ gas dilution (70% dilution $H_2$-$H_2S$: 7-3 sccm and ~81% dilution, $H_2$-$H_2S$: 30-7 sccm, Figure S1c and Figure S1d, respectively) led to a significant change in surface morphology, with the nanoflakes now transformed into fin-like structures. In addition to the strong (002) peak, an additional peak corresponding to the (010) crystal plane was observed (Figure S1f), which suggested the growth of crystalline $WS_2$ with a different texture in comparison with the aforementioned cases (no dilution, 0-10 sccm and 30% dilution, 3-7 sccm). Further increasing the $H_2$ dilution (~94% dilution, 30-2, Figure S1f) led to an increase in the intensity of the (010) peak, thus, enhancing the degree of preferential orientation. This was accompanied by sharpening of the fin-like structures as observed in Figure S1e.

Due to the contrasting material properties in terms of surface morphology and texture, which could influence the HER performance, the flow rates of '0-10 (no $H_2$ dilution) and 30-2 (~94% $H_2$ dilution)' were selected for further studies. As mentioned in the main text, the $H_2$-$H_2S$ gas flow into the ICP source was always accompanied with Ar gas (40 sccm).

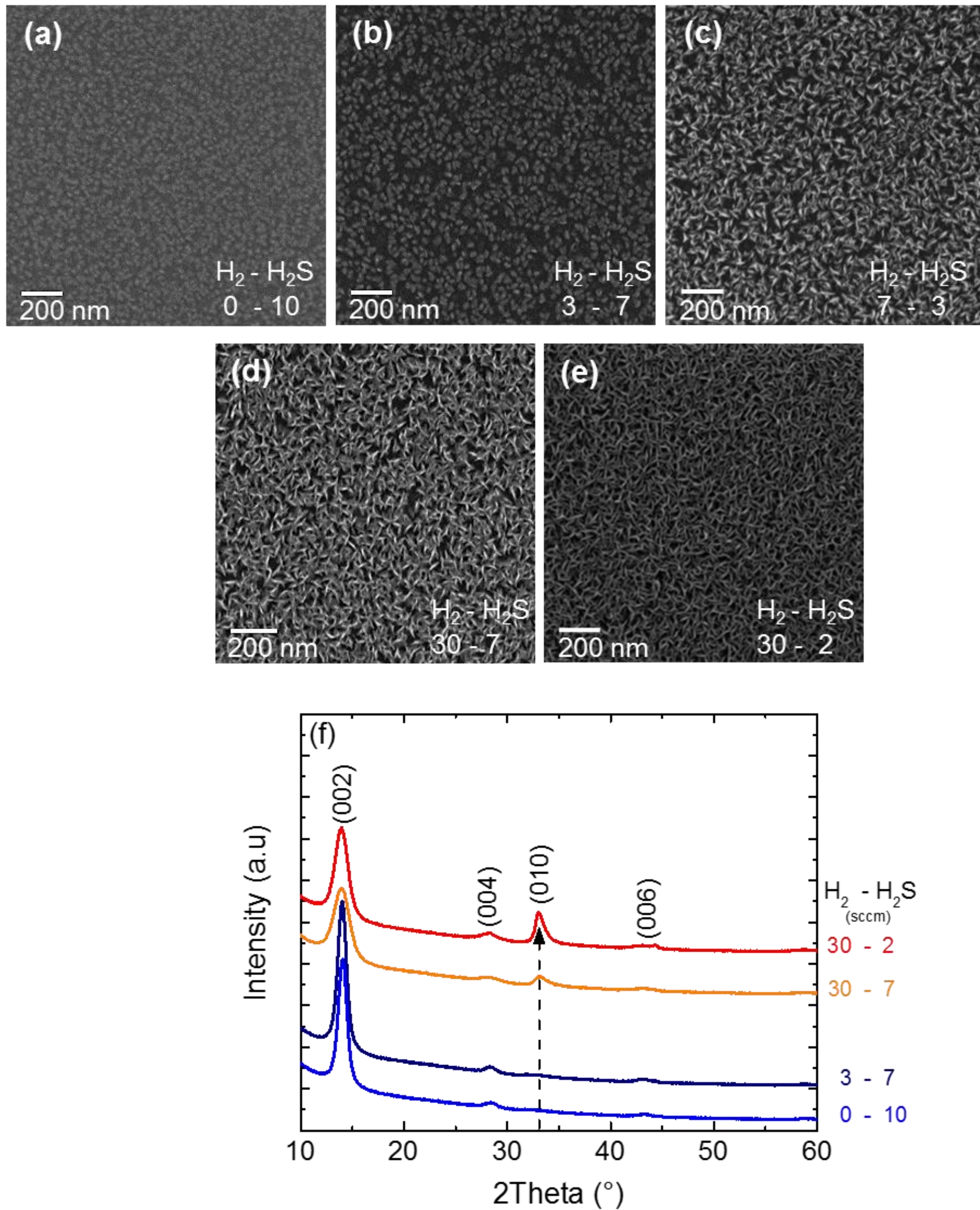


Figure S1. (a-e) SEM images of $WS_2$ after 200 PEALD cycles deposited with different $H_2$ - $H_2S$ plasma gas mixture flow rates: (a) 0-10, (b) 3-7, (c) 7-3, (d) 30-7 and (e) 30-2. (f) Gonio-XRD diffractograms of $WS_2$ films deposited with different $H_2$-$H_2S$ plasma gas mixture flow rates.

<u>$WS_2$ PEALD saturation curves</u>

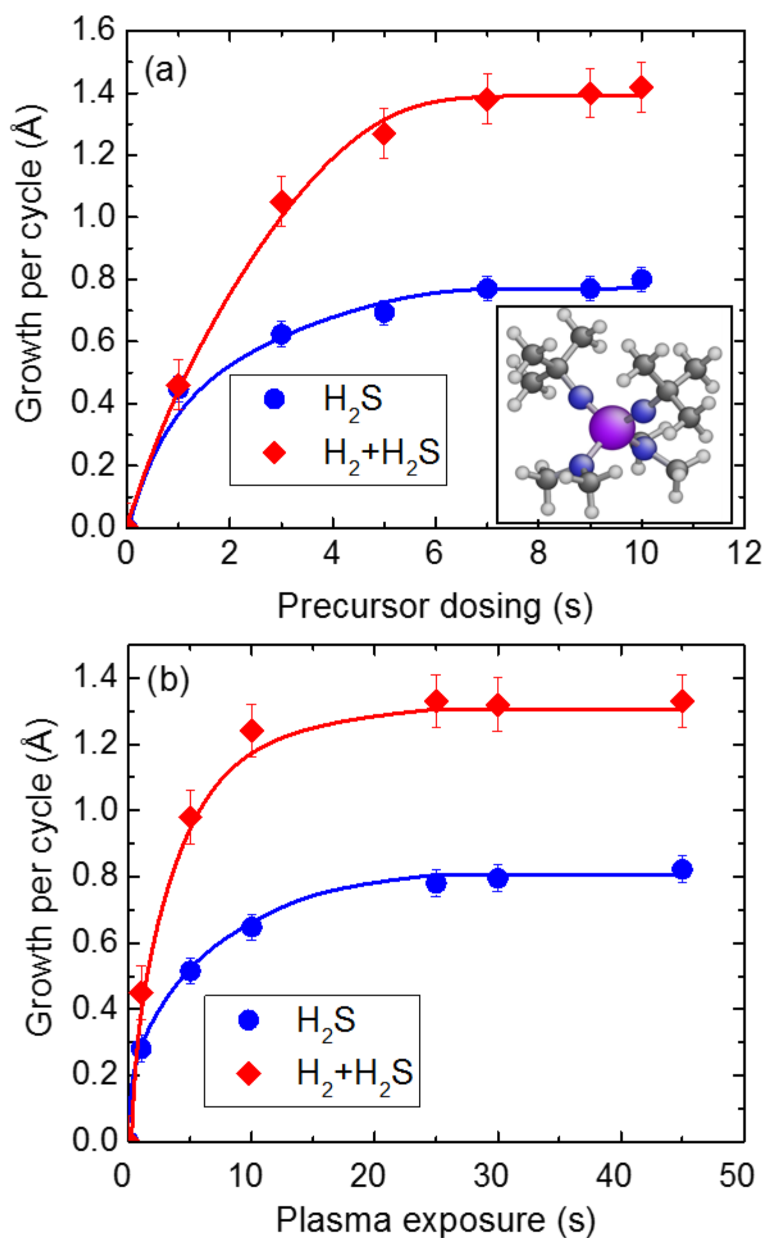


Figure S2. $WS_2$ PEALD saturation curves showing the GPC as a function of (a) precursor dosing (precursor molecule in inset) and (b) co-reactant plasma exposure for the $H_2S$ (blue circles) and $H_2$+$H_2S$ process (red diamonds). The solid lines serve as a guide to the eye.

The plots in Figure S2 show the self-limiting ALD growth behaviour observed during the (a) precursor dosing and (b) plasma exposure half cycles for the $H_2S$ and $H_2$+$H_2S$ processes at 300 °C. For precursor saturation studies (Figure S2a), the plasma exposure was fixed at 30 s while varying the precursor dose. For plasma saturation studies (Figure S2b), the precursor dose was fixed at 10 s while varying the plasma exposure. For all the PEALD experiments reported in the main text, a precursor dosing time of 10 s was adopted in order to ensure that GPC is well in saturation, although, the GPC appeared to saturate already at around 6 s (Figure S2a). Similarly, the $H_2S$ plasma exposure was fixed at 30 s although the GPC appeared to saturate

already at around 20 s (Figure S2b). For the $H_2$+$H_2S$ process, the error in GPC determination is relatively higher owing to the rough surface morphology.

## XPS analysis

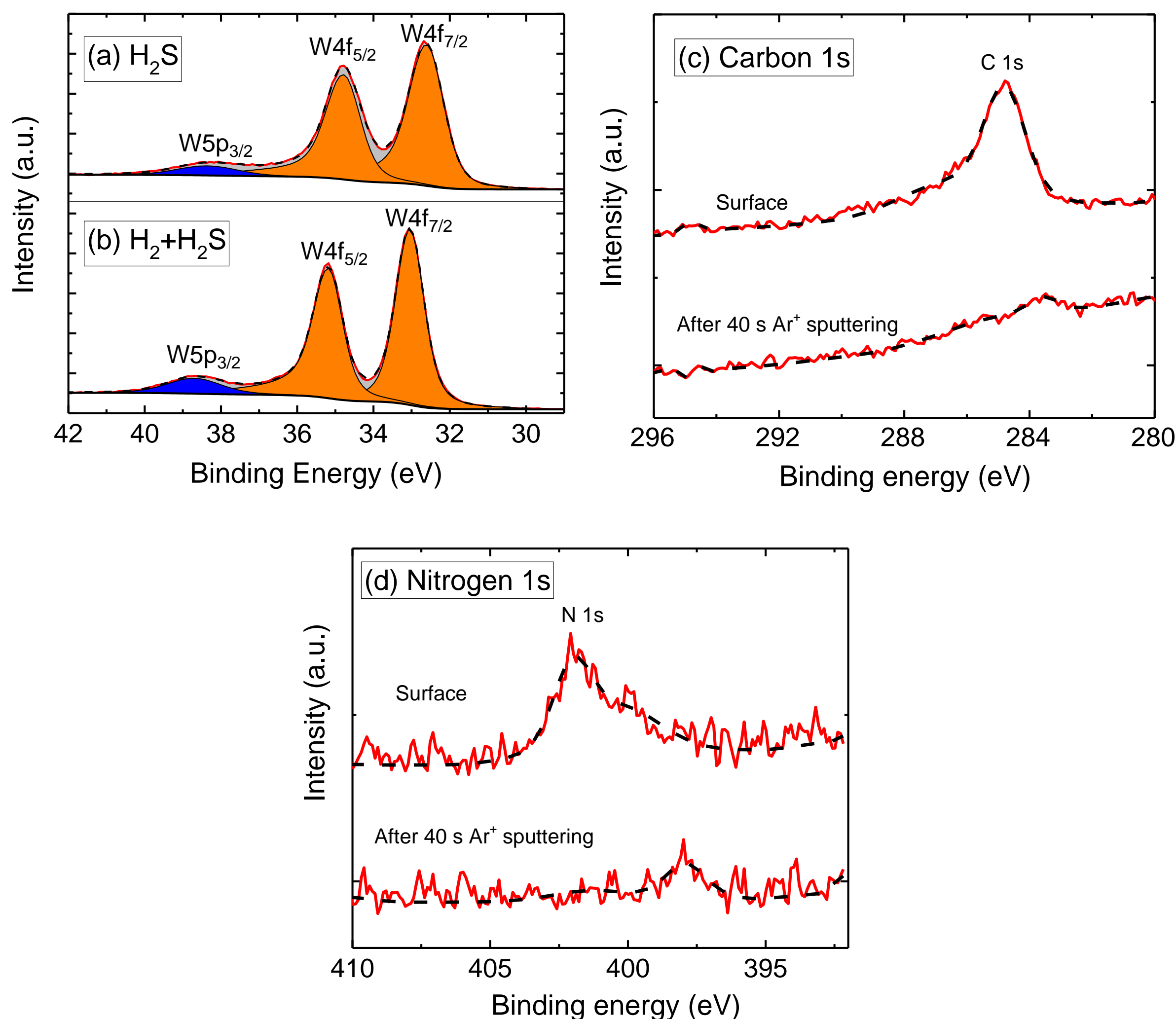


Figure S3. Resolved tungsten 4f core level spectra as determined from XPS measurements for the $WS_2$ films grown using the (a) $H_2S$ and (b) $H_2$+$H_2S$ processes, respectively. The red solid lines indicate the raw experimental data and the dashed black lines indicate the fit. The XPS peak fitting for the W4f doublet was performed with two constraints: intensity ratio of 0.75 and binding energy difference of 2.17±0.2 eV between the W4f$_{5/2}$ and W4f$_{7/2}$ orbital. (c) Carbon 1s and (d) nitrogen 1s peak observed on the surface, which disappeared after depth profiling with Ar ions (energy =500 eV) for 40 s for the $WS_2$ films grown using the $H_2S$ process.

Table S1. The stoichiometry of $WS_2$ films deposited using $H_2S$ and $H_2$+$H_2S$ processes as obtained from XPS and RBS measurements.

| PEALD process | S:W (XPS) | S:W (RBS) |
|---|---|---|
| $H_2S$ | 2.35±0.15 | 2.20±0.10 |
| $H_2$+$H_2S$ | 1.92±0.10 | 1.80±0.10 |

## Optical emission spectroscopy of the $H_2S$ based plasmas

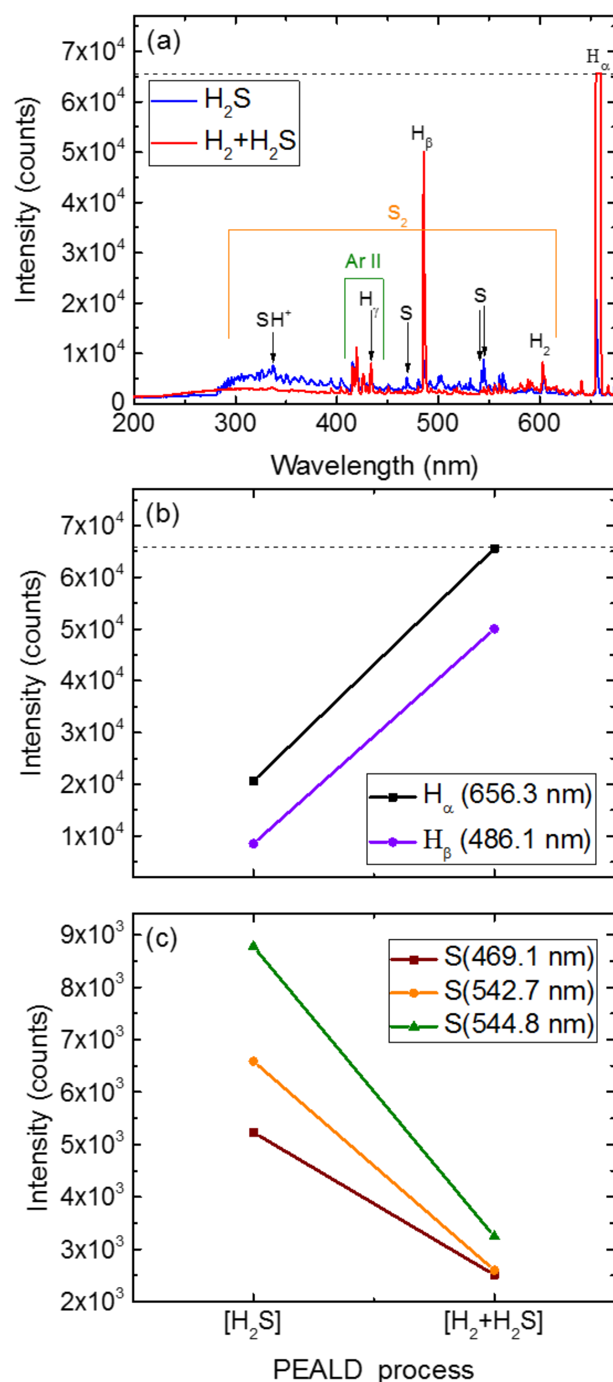


Figure S4. (a) Optical emission spectra of the $H_2S$ and $H_2$+$H_2S$ plasmas that were utilized in this work.[1–3] The atomic hydrogen, atomic sulfur, and the $H_xS_y$ emissions are highlighted in the spectra. The respective intensities of the (b) atomic hydrogen lines and (c) atomic sulfur lines are compared for both plasmas. The dashed lines in (a) and (b) indicate the OES detector saturation and the $H_\alpha$ emission line intensity was found to be beyond the maximum detection range of the detector. The optical emission spectra acquisition parameters were optimized such that the relevant peaks with varying intensities could be detected for the utilized ALD reactor and OES detector configuration. The Ar emission lines (696 and 707 nm, data not shown) exhibited comparable intensities (696 nm ~5.3 x $10^4$ counts and 707 nm ~ 6 x $10^4$ counts) in both the plasmas.

# Computational Section

## (a) Computational details

In order to investigate the chemical reactivity of different facets toward the W precursor, we built two simulation boxes as shown in Figure S5. The first simulation box (Figure S5a) represents the basal plane (crystalline {001} facet of $WS_2$). Converged values of the surface energies of the $WS_2$ show that three layers of $WS_2$ {001} is enough to be considered as slab. For this surface, we use a 5x5x1 supercell to include the bulky precursor. Therefore, the simulation box contains 272 atoms, including the W precursor (Figure S5a). To avoid slab-slab interaction in the periodic model, a vacuum region of 20 Å above the surface is imposed for both the simulation boxes.

The second simulation box (Figure S5b) represents the edge structure (crystalline (010) surface of $WS_2$). Converged values of the surface energies shows that four layers of $WS_2$ (010) surface is enough to be considered as a slab. The cleavage of (010) facet terminates to the bare W atoms. To follow the course of ALD reactions, we remove the bare W from this facet and then expand the slab to build the surface. For the surface, we use a 1x4x1 supercell to include the bulky precursor. Therefore, the simulation box has 183 atoms in total. This includes the W precursor (Figure S5b).

The *k*-point sampling in reciprocal space is performed by the Monkhorst–Pack method. 6x6x6 grid size is enough to utilize for the bulk optimization. 6x6x1 and 3x3x3 grid sizes are utilized for the slab of basal plane and edge structure, respectively. The k-point sampling is reduced to 1x1x1 for both simulation boxes.

The edge structure consists of two layers of $WS_2$ (Figure S5a) in which four W atoms are located in the sub-layer. Therefore, in total 8 W and 16 S atoms are located at the edge surface. The SH-coverage is calculated as the ratio of SH atoms to W atoms in the first simulation box. Each layer of the basal plane in the second slab has 25 W atoms and is considered as a mono-layer (ML). The coverage of SH-atoms is similarly calculated based on the number of SH-atoms divided by the number of W atoms in a ML.

To generate the different SH-coverage at the surface, we assumed that either 2H atoms have been removed as molecular $H_2$ or 2H and S atoms have been removed as $H_2S$ molecule. In both cases, the desorbed molecule are closed shell molecule. Therefore, we keep the simulation boxes neutral.

To include van der Waals (vdW) interactions, the vdW functional 'optPBEvdW'[4,5] was chosen to treat the adsorption energy of the W precursor at the $WS_2$ surface, since there is good agreement between the vdW functionals (opt) and the random phase approximation (RPA) calculation. As a general trend, the inclusion of vdW interactions makes the adsorption energy more negative.

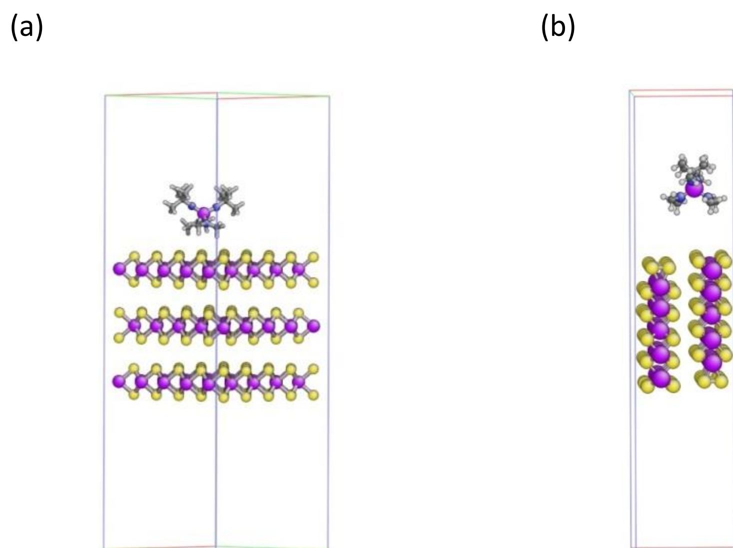


Figure S5. (a) Represents the interaction of the $W(NMe_2)_2(N^tBu)_2$ precursor with the pristine basal plane of $WS_2$ (crystalline {001} facet). This simulation box contains 272 atoms. (b) Represents the interaction of the W precursor with the edge structure of $WS_2$ (crystalline {010}) facet). This simulation box contains 183 atoms. (violet=W, yellow=S, dark blue=N, white=H, dark gray=C).

## (b) Adsorption of W precursor on the basal plane – {001} facet

To investigate the adsorption of the W precursor on the reduced basal plane, S atoms were randomly removed from the surface. Removed S atoms also render the W atom accessible to the $WX_2Y_2$ precursor. Since W deficiencies were not observed experimentally, they were not considered in our calculations.

As a general trend, H-atoms also intended to desorb as molecular $H_2$ at the reduced basal plane. In some case (Figure S6b), when there was no thiol group (-SH) in neighbouring H-atoms, single H-atom bonded to S and remained at the surface (Figures S6d and S6e). Hence, the W precursor was introduced to both S and W atoms at the basal plane with different SH-coverage (Figure S6).

The introduction of W precursor to the S atom at the reduced basal plane did not give rise to chemical adsorption. The precursor only physically adsorbed at the S atom (Figure S6a and S6b). The adsorption was exothermic by 0.02 eV at 0.6 ML S and endothermic by 0.27 eV at 0.8 ML S and 0.4 ML H (Table S2, reaction 1 and 2). The inclusion of vdW interaction did not lead to a large difference. The aforementioned reactions were exothermic by 0.31 eV and 0.39 eV, respectively upon inclusion of vdW interactions.

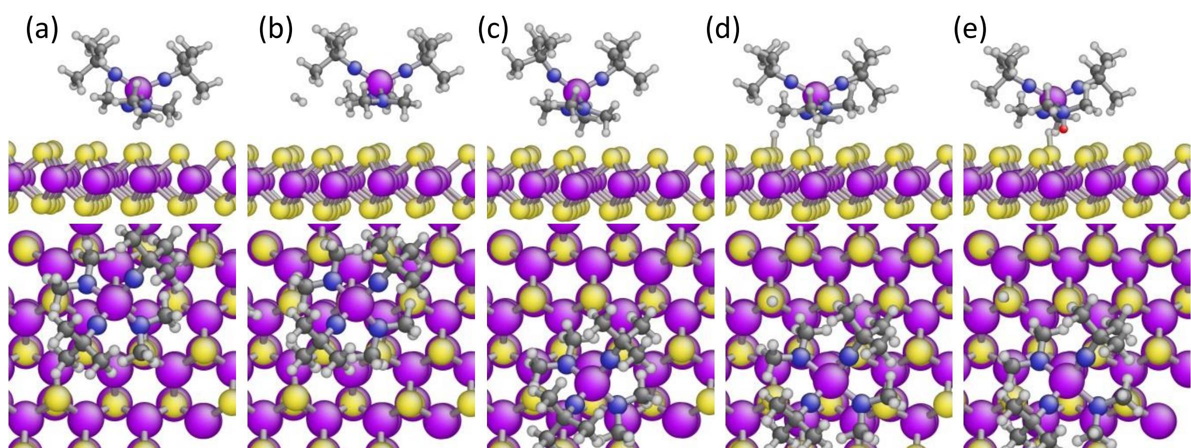


Figure S6. Physical adsorption of $WX_2Y_2$ at the reduced surface of $WS_2$ ({001}), including vdW interactions (side view). The W precursor is introduced to the both S and W atom at the different SH-coverage (top view). (a) and (b) correspond to the reaction 1 and 2 while (c) to (e) correspond to the reaction 3 to 5 in Table S2.

In the next step, the W precursor was introduced to the W atom at the reduced surface of $WS_2$ {001}. The adsorption was endothermic by 0.31 eV at 0.6 ML S (Figure S6c) and endothermic by 1.68 eV at 0.8 ML S and 0.4 ML H (Figure S6d) (Table S2, reaction 3 and 4). The inclusion of vdW interaction made the aforementioned adsorption exothermic by 0.71 eV and 0.31 eV, respectively. The introduction of W precursor did not give rise to a chemical adsorption of W precursor (Figure S6).

As mentioned above, there is a minor case that H-atom remains at S atom which is close to the S defects. If proton is being accessible to the dimethylamido ligand of the introduced W precursor, then proton transfer could lead to a strong adsorption of the W precursor (Table S2, reaction 5). This adsorption is exothermic by 2.12 eV. This could be considered as a seed precursor for the nucleation and consequently formation of a new layer (Figure S6e).

Table S2. Adsorption energies of W precursor for different SH-coverages on the $WS_2$ basal planes ({001} facet). The dimethylamido ligand and the tert-butylimido ligand are shown by $X=N(CH_3)_2$ and $Y=NC(CH_3)_3$, respectively. $^*$shows the physisorbed precursor. ΔE for reaction 5 could not be determined.

| Reaction | SH-coverage | $\Delta E$ (eV) | $\Delta E$ (eV) including vdW |
|---|---|---|---|
| 1. $WX_2Y_2(g)+S(s) \rightarrow WX_2Y_2^*+S(s)$ | 0.6 ML S and 0.0 ML H | -0.02 | -0.31 |
| 2. $WX_2Y_2(g)+S(s) \rightarrow WX_2Y_2^*+S(s)$ | 0.8 ML S and 0.4 ML H | 0.27 | -0.39 |
| 3. $WX_2Y_2(g)+W(s) \rightarrow WX_2Y_2^*+W(s)$ | 0.6 ML S and 0.0 ML H | 0.31 | -0.71 |
| 4. $WX_2Y_2(g)+W(s) \rightarrow WX_2Y_2^*+W(s)$ | 0.8 ML S and 0.4 ML H | 1.68 | -0.31 |
| 5. $WX_2Y_2(g)+SH(s) \rightarrow WHX_2Y_2^*+S(s)$ | 0.8 ML S and 0.4 ML H | -- | -2.12 |

## (c) Complementary Calculations: Proton transfer and reduction of $WS_2$ edge structure

The adsorption of precursor and protonation of ligand are often considered as distinct reaction steps. Here, we observed that the proton transfer occurs during the adsorption of W precursor

on the $WS_2$ edge structure ({010} facet). The proton transfer depends on the accessibility of H-atoms at the surface to the ligands of precursor. To distinguish the adsorption of precursor and proton transfer, we reorder H-atoms at the surface in such a way to be accessible to N of dimethylamido ligand or not. The reordering has been done by hand for the same SH-coverage. In addition, we calculated the adsorption energy in the presence and absence of vdW interaction.

When the H-atom is accessible to the N, the proton transfer is barrier-less and it occurs during the adsorption. Figure S7a and b show the strong adsorption of W precursor at the edge structure of $WS_2$ at the H-coverage of 1.0 ML and 1.5 ML, respectively. In the presence of vdW, this proton transfer makes a large contribution (>1.0 eV) in the adsorption energy.

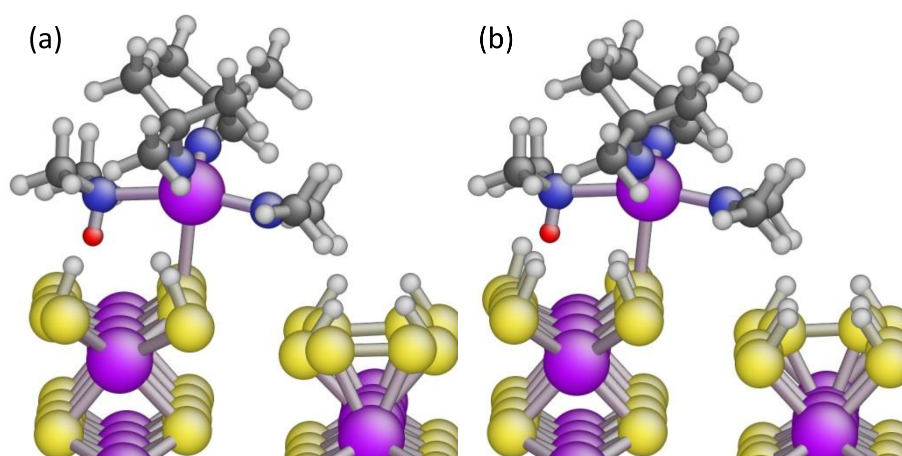


Figure S7. Chemical adsorption of the W precursor at the full S-coverage of 2 ML with the H-coverage of 1.0 ML (a) and the H-coverage of 1.5 ML (b), corresponding to the reactions 6 and 7 in Table 2 in manuscript, respectively. The vdW interaction is included for both configurations. The colour code is the same as Figure S5. The transferred proton is identified by a red sphere.

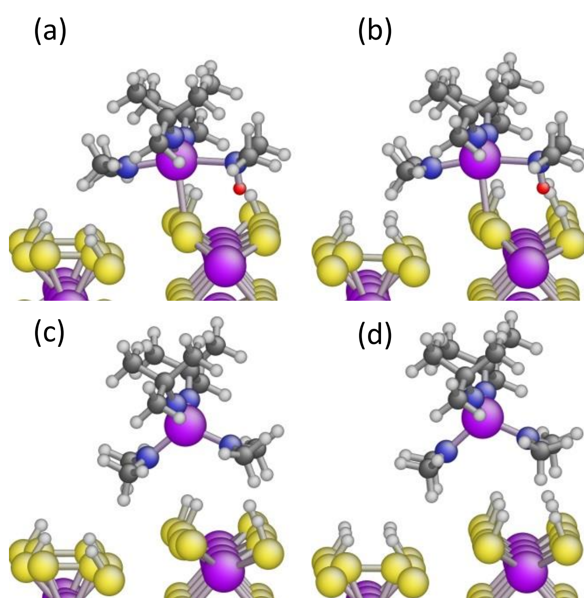


Figure S8. Chemical adsorption of the W precursor due to the proton transfer to the dimethylamido ligand at the full S-coverage of 2 ML with the H-coverage of 1.0 ML (a) and the H-coverage of 1.5 ML (b). If proton transfer does not occur, the W precursor only physically adsorbed at the above

coverages, the SH-coverage at (c) and (d) are corresponding to (a) and (b), respectively. The vdW interaction is not considered in all configurations.

In the absence of vdW interactions, similar proton transfer is observed during the adsorption of precursor, if the H-atom at the surface is accessible to the N (Figure S8a and b). This proton transfer makes a small contribution (<0.1 eV) in the adsorption energy. If the proton is not accessible to the N, the W precursor only physically adsorbed to the surface in the absence of vdW interactions (Figure S8c and d).

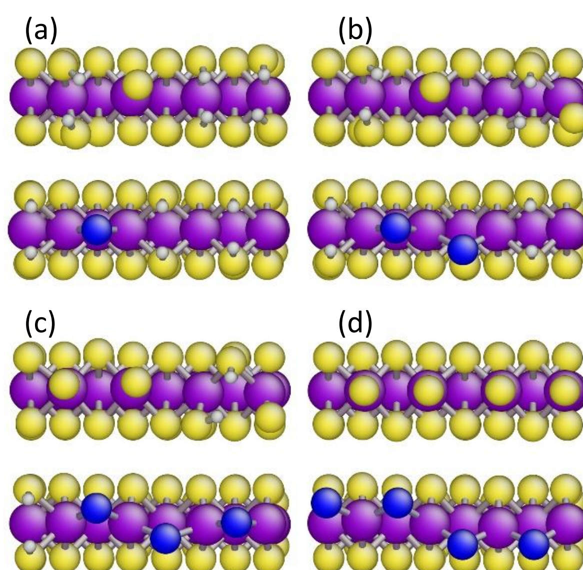


Figure S9. Reduction of the edge structure of $WS_2$ from (a) to (d), corresponding to the reaction 8 to 11 in Table 2 in the main text. Desorption of $H_2S$ molecules leads to the relocation of more S atoms to the bridging sites (a) to (d) (blue element). Due to the relocation of S atoms, the W surface atoms remained inaccessible to the W precursor at the S-coverage of 1ML.

## TEM images of $WS_2$ ($t_{App}$~64 nm) synthesised using $H_2$+$H_2S$ process

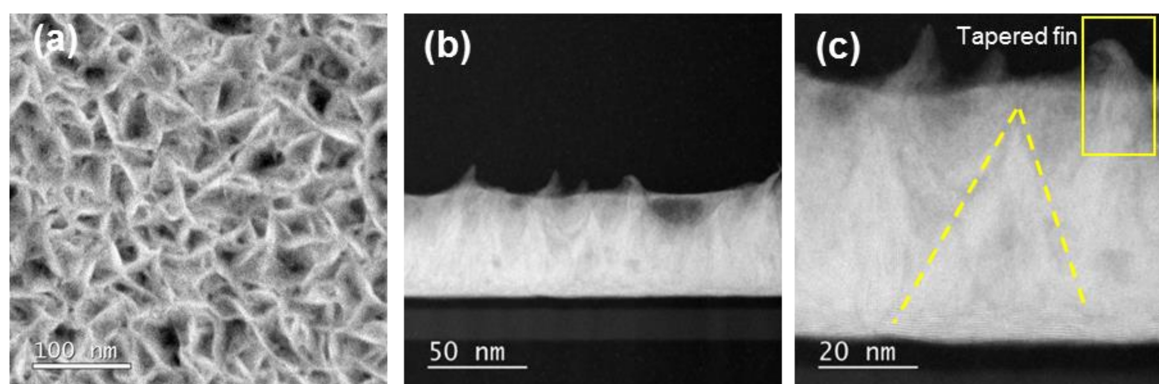


Figure S10. TEM images of $WS_2$ ($t_{App}$~64 nm): (a) Top-view and (b and c) cross section images of $WS_2$ grown using the $H_2$+$H_2S$ process. A tapered fin on the top surface is highlighted with a rectangle around it and the dashed lines follow the triangular-fin outline in the magnified image (c). The triangular fin is projected onto other, differently oriented fins as the sample thickness is larger than the lateral fin dimensions.

# Film properties of $WS_2$ ($t_{App}$~64 nm) synthesised using $H_2$+$H_2S$ process

Table S3. Film composition and mass density of $WS_2$ (~64 nm thick) grown $H_2$+$H_2S$ PEALD process. The stoichiometry and number of deposited W atoms per $nm^2$ per cycle, were deduced from RBS measurements while the atomic hydrogen content was determined from ERD measurements. The mass density was determined by combing the RBS results and *in situ* SE determined thickness.

| PEALD process | S:W | W (atom/($nm^2$ cycle)) | [H] at.% | Mass density ($g/cm^3$) |
|---|---|---|---|---|
| $H_2$+$H_2S$ | 1.9±0.1 | 1.95±0.05 | 10.3±0.5 | 5.0±0.5 |

# Copper UPD – evaluation of the number of active sites

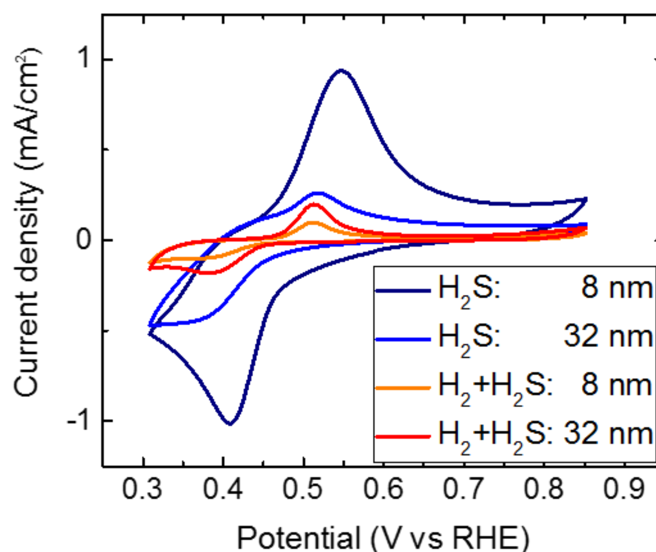


Figure S11. Cyclic voltammetry showing the underpotential deposition regions between 460 to 610mV for the $WS_2$ films on glassy carbon substrates in 0.002M CuSO4 and 0.1M $H_2SO_4$with a scan rate of 50 mV/s.

The number of active sites was determined using the method adopted by Voiry et al.[6] The amount of charges generated during Cu stripping ($Q_{Cu}$) was calculated by integrating the area under the Cu stripping peak (460-610 mV). From this we could calculate the amount of copper deposited:

$$amount\ of\ deposited\ Cu\ (mol\ per\ geometric\ area) = \frac{Inegration\ area\ of\ Cu\ stripping}{96500*2*Scan\ rate}$$

and the number of active sites per geometric area (number of deposited Cu atoms per geometric area) was determined by multiplying the above equation with the Avogadro's number ($6.023*10^{23}$ $mol^{-1}$). As mentioned in the manuscript, to account for background

correction, charges obtained from the electrode in 0.1 M $H_2SO_4$ (without $Cu^{2+}$) were subtracted from the charges obtained for copper stripping.

# Surface morphology of $WS_2$ on different substrates

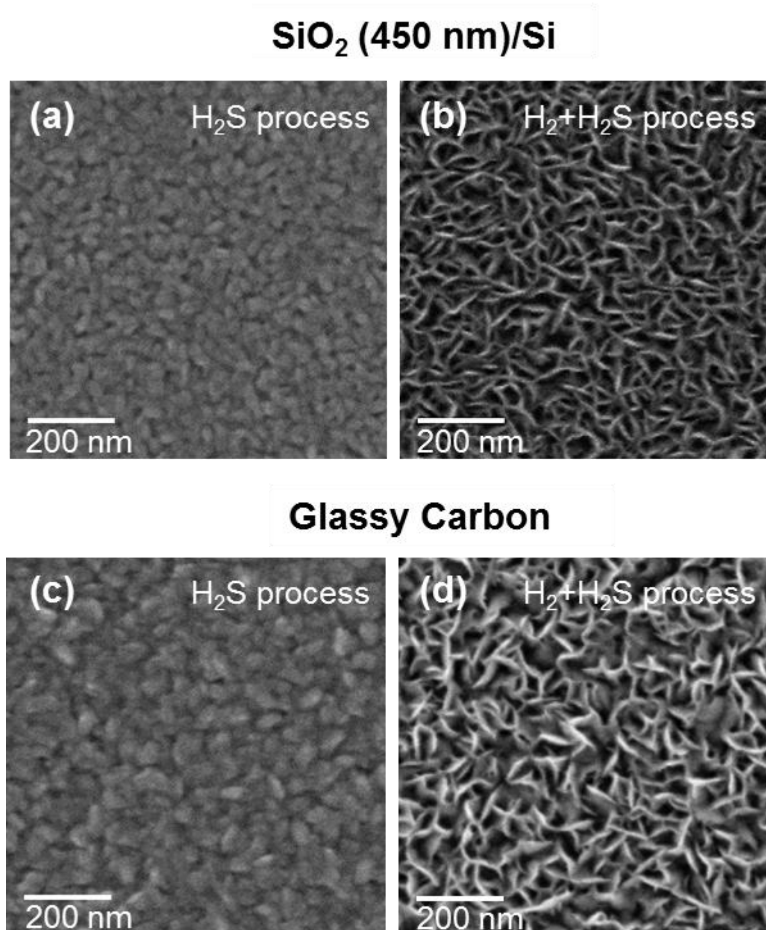


Figure S12. SEM images showing the identical surface morphology of $WS_2$ with comparable thickness ($t_{App}$~32 nm) deposited using $H_2S$ and $H_2$+$H_2S$ process on: (a, b) Si substrate with 450 nm thermally grown $SiO_2$ and (c, d) glassy carbon substrates.

## Blocking of layers in $WS_2$ film

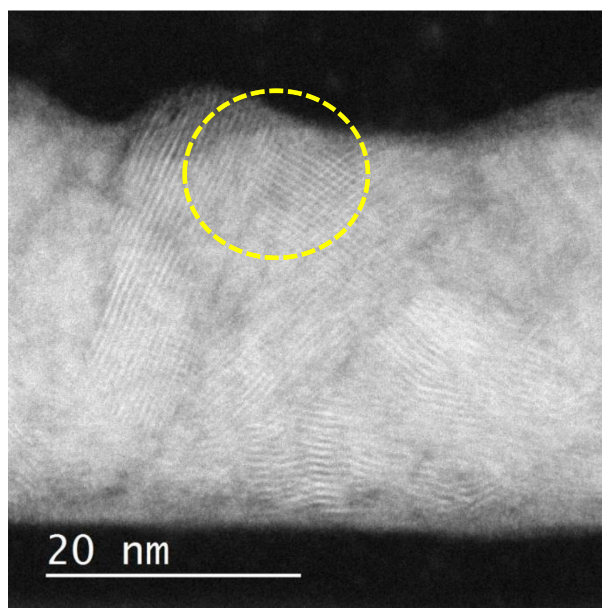


Figure S13. TEM image displaying the blocking (highlighted by the yellow circle) of obliquely angled (non-vertical) layers in the $WS_2$ film ($t_{App}$~32 nm) grown using the $H_2S$ process.

## Electrochemical impedance spectroscopy data

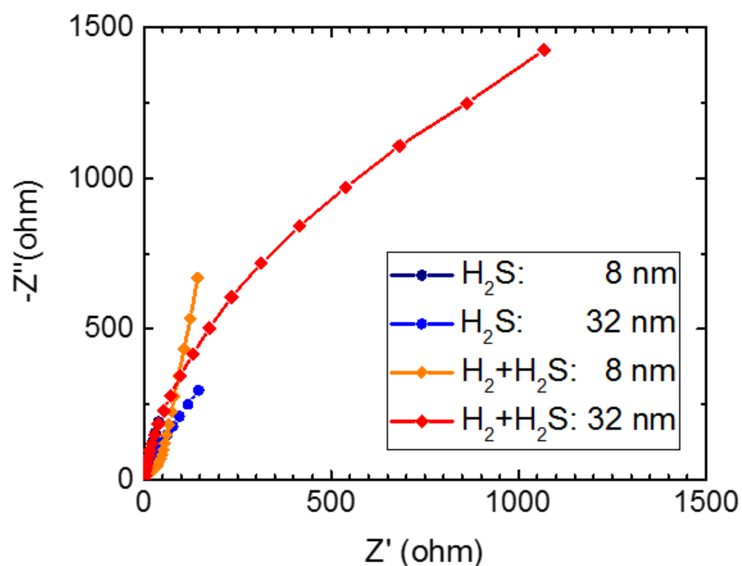


Figure S14. Electrochemical impedance spectroscopy (EIS) data of $WS_2$ films deposited using $H_2S$ and $H_2$+$H_2S$ process on glassy carbon substrates. The EIS was recorded at open circuit potential over a frequency range of 1 Hz to 100 kHz. For the $WS_2$ films grown using the $H_2S$ process with thickness ($t_{App}$) of ~8 and ~32 nm the Z' values are ~40 and ~140 Ω, respectively. For the $WS_2$ films grown using the $H_2$+$H_2S$ process with thickness of ~8 and ~32 nm the Z' values are ~140 and ~1070 Ω, respectively.

**References**

(1) R. W. B. Gaydon and A. G. Pearse. *The Identification of Molecular Spectra*; Chapman and Hall: London, 1950.

(2) Kosaraju, S.; Marino, J. A.; Harvey, J. A.; Wolden, C. A. Plasma-Assisted Co-Evaporation of β-Indium Sulfide Thin Films. *Sol. Energy Mater. Sol. Cells* **2006**, *90* (7–8), 1121–1135.

(3) Kuhs, J.; Hens, Z.; Detavernier, C. Plasma Enhanced Atomic Layer Deposition of Aluminum Sulfide Thin Films. *J. Vac. Sci. Technol. A Vacuum, Surfaces, Film.* **2018**, *36* (1), 01A113.

(4) Klimeš, J.; Bowler, D. R.; Michaelides, A. Chemical Accuracy for the van Der Waals Density Functional. *J. Phys. Condens. Matter* **2010**, *22* (2), 022201.

(5) Klimeš, J.; Bowler, D. R.; Michaelides, A. Van Der Waals Density Functionals Applied to Solids. *Phys. Rev. B* **2011**, *83* (19), 195131.

(6) Voiry, D.; Yamaguchi, H.; Li, J.; Silva, R.; Alves, D. C. B.; Fujita, T.; Chen, M.; Asefa, T.; Shenoy, V. B.; Eda, G.; et al. Enhanced Catalytic Activity in Strained Chemically Exfoliated $WS_2$ Nanosheets for Hydrogen Evolution. *Nat. Mater.* **2013**, *12* (9), 850–855.